ACS APPLIED NANO MATERIALS
Cite This: ACS Appl. Nano Mater. 2019, 2, 1828−1843
Article
www.acsanm.org

Particle Size, Morphology, and Chemical Composition Controlled $CoFe_2O_4$ Nanoparticles with Tunable Magnetic Properties via Oleic Acid Based Solvothermal Synthesis for Application in Electronic Devices

Sumayya M. Ansari,[†] Bhavesh B. Sinha,[‡] Deodatta Phase,[§] Debasis Sen,[∥,⊥] Pulya U. Sastry,[∥,⊥] Yesh D. Kolekar,[*,†] and Chintalapalle V. Ramana[*,#]

[†]Department of Physics, Savitribai Phule Pune University, Pune 411007, India
[‡]National Center for Nanoscience and Nanotechnology, University of Mumbai, Mumbai 400098, India
[§]UGC-DAE, Consortium for Scientific Research, Khandwa Road, Indore 452001, India
[∥]Solid State Physics Division, Bhabha Atomic Research Centre, Mumbai 400085, India
[⊥]Homi Bhabha National Institute, Anushaktinagar, Mumbai 400094, India
[#]Center for Advanced Materials Research (CMR), University of Texas at El Paso, 500 W. University Avenue, El Paso, Texas 79968, United States

Supporting Information

ABSTRACT: We report on the realization of particle size, morphology, and chemical composition controlled cobalt ferrite nanoparticles (CFO NPs) with tunable magnetic properties for application in electronic and electromagnetic devices. The effect of oleic acid concentration (0.0−0.1 M) on the structural, physical, chemical, electronic, and magnetic properties of solvothermally synthesized CFO NPs is investigated in detail by using the oleic acid (OA) based chemical method for synthesis. Crystalline, cubic, and chemically homogeneous CFO NPs (5−15 nm) can be obtained by controlling the OA concentration. Spectroscopic analyses revealed that the OA molecules form covalent bonds with CFO NPs. The particle-size control was achieved by bridging bidentate interactions between the OA molecules and CFO NPs. Detailed magnetic measurements revealed that the OA concentration helps to effectively control the magnetic behavior of particle-size-controlled CFO NPs. The interfacing between OA molecules and CFO surface atoms leads to modified magnetism which is the key to understand the underlying mechanisms and utilize magnetic nanoparticles in practical applications. The anisotropy constant variation directly with nanoparticle size indicates that the magnetocrystalline component governs the magnetic anisotropy in OA coated CFO. Removal of OA (after thermal treatment) induces enhanced magnetic anisotropy and exchange bias as consequence of surface component. The results and analyses suggest that the molecular coating of nanoparticles offers the most important and critical step to design novel nanostructured magnetic materials for current and emerging electronic device technologies.

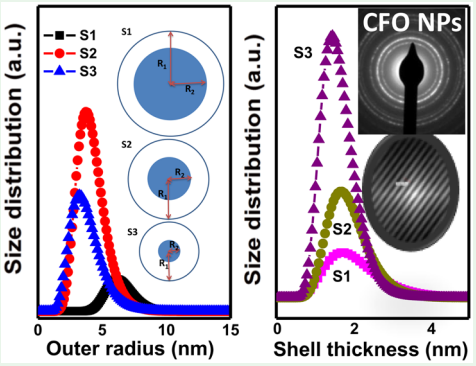

KEYWORDS: *cobalt ferrite, nanoparticles, surface coating, oleic acid, structure, magnetism*

I. INTRODUCTION

Magnetic nanostructured cobalt ferrite, $CoFe_2O_4$ (CFO), has the vast potential for applications in several technologies.[1−10] CFO nanoparticles (NPs) and nanomaterials find application in magnetic hyperthermia, molecular imaging, electronics, spintronics, information storage, supercapacitors, drug delivery, magnetic resonance imaging, and catalysis.[1−8] Recently, nanostructured CFO has been proposed as a candidate material for the field emission based electronic display devices.[3] By virtue of exceptional cubic magnetocrystalline anisotropy, which is (1.8−3.0) × 10^6 erg/cm^3, and tunable electrical properties, CFO NPs have been widely considered for integration into many of the current and emerging electronic and electromagnetic device applications.[1−10] Most recently, CFO NPs have been attracting the attention of scientific and research community for their effective utilization in flexible and organic electronics, specifically in field effect transistors (FETs) and memory devices for high-performance computing.[9,10] For instance, functionalization of diphenylalanine-based self-assembled nanotubes with CFO magnetic NPs

Received: November 7, 2018
Accepted: February 26, 2019
Published: February 26, 2019

DOI: 10.1021/acsanm.8b02009
ACS Appl. Nano Mater. 2019, 2, 1828−1843

provides an approach to realize the organic FETs with much lower operating voltages.[9] Also, realization of high-performance nanofloating gate memory (NFGM) devices (transistor type memory devices) has been reported using CFO NPs as an active dielectric in an organic−inorganic based multilayered device.[10] It has been reported that, compared to other metal oxide NPs, the tunable electrical conductivity, excellent chemical stability, and mechanical strength of $CoFe_2O_4$ NPs account for their enhanced performance in these transistor-type memory or NFGM devices.[10] It must be noted that for electronic and electromagnetic applications such as emission displays, electron sources in electron microscopes, X-ray sources, and memory-based electronic devices, optimum or enhanced device performance can be achieved by controlling the morphology, particle size, and composition of nanoscale materials.[3,10]

In all of the aforementioned electronic devices and related applications, especially in the emerging field of flexible electronics and electromagnetics, the following approaches were considered to effectively control the structure and enable practical utilization of MNPs: (a) interfacing the surface layers with MNPs; (b) functionalization or forming composites with MNPs; (c) coatings as a protective layers on the MNPs. However, it is well-known that the magnetic interactions, where NPs' surface atoms dominate functional activity,[1−3] play a major role in governing the underlying science of nanoscale magnetic systems. In addition, it has been reported that the interparticle interactions strongly influence the magnetic behavior of NPs and its assembly.[14] The application of MNPs is always a concern; concentrated assemblies of individually responding magnetic entities are required.[1−3] However, it is difficult to meet the condition due to the fact that interparticle dipole−dipole interactions are strongly enhanced by increasing MNPs' size and/or concentration.[15] Therefore, surface coating of NPs represents a useful and valuable tool to control their properties and prevent NPs aggregation. However, detailed studies on this subject are rather poor while some contradictory results exists.[15−17] The coating materials (molecules) can modify the structural, chemical, electrical, and magnetic properties of core NPs;[11−13,17−19] it has been widely documented in the literature that the coatings and/or surfactants change particle interactions, surface anisotropy, and saturation magnetization.[17−19]

Using oleic acid (OA) is an effective approach for coating of particles.[20] Existing few studies on OA coated iron oxides demonstrate strong effect on their magnetic properties.[21−23] However, these studies cannot be considered conclusive in terms of particle size−composition−property correlation due to the fact that the investigated and compared CFO NPs are not prepared by the same chemical route.[21−26] Furthermore, it is well-known that synthetic methods and various experimental conditions can strongly affect the individual particle size, particle distribution, and morphology of the NP system. While the effects of OA on the properties of resulting materials are extensively investigated, evidence on the effect of OA concentration on the crystal growth, surface/interface chemistry, and agglomeration of CFO NPs remains scarce. In this context, we aim to develop a better and deeper understanding of the OA effect on the crystal structure, morphology, chemical bonding, electronic structure, and magnetic properties of CFO. To achieve this scientific goal, we performed a systematic, comprehensive investigation using a wide variety of advanced microscopic and spectroscopic analytical methods to explore the effect of OA concentration on the physicochemical properties of CFO NPs synthesized by solvothermal method. Our results demonstrate that the increasing OA concentration induces the particle size reduction, which in turn effectively controls the strength of dipolar interparticle interactions in CFO NPs and dictates their magnetic properties. Moreover, the CFO NPs synthesized using the present approach exhibit the remarkably higher coercivity values compared to bulk CFO in addition to OA concentration facilitating the tuning of structure and magnetic properties, which may be quite useful for the aforementioned electronic device applications. The results obtained are presented and discussed to establish the particle size−composition−magnetic property correlation in CFO NPs synthesized by the OA mediated solvothermal process.

II. EXPERIMENTAL DETAILS

A. Sample Preparation. The CFO NPs were synthesized using the solvothermal approach by varying the OA concentration. All the analytical grade (AR) reagents (Sigma-Aldrich) were used as received. During the preparation, cobalt nitrate ($Co(NO_3)_2{\cdot}6H_2O$) and iron nitrate ($Fe(NO_3)_3{\cdot}9H_2O$) in stoichiometry proportion (1:2) were added to ethylene glycol (EG) solution, and the mixture was stirred well. By adding urea solution and then OA drop-by-drop, pH of solution was adjusted to 12 and total solution volume as 2/3 of the total volume of autoclave (250 mL). After that, the solution mixture was treated under solvothermal condition at 180 °C for 24 h. The particles were then separated by centrifuge using the final solution with DI water and ethanol several times. The resulting black precipitates were dried (overnight) in an oven at 100 °C. Following the same procedure, CFO NPs with 0.01, 0.05, and 0.1 M OA were synthesized and denoted as S1, S2, and S3, respectively.

B. Characterization. *Thermogravimetric Analysis (TGA).* Thermogravimetric analysis (TGA, METTLER TOLEDO) was employed to obtain the percentage of OA present on the NPs surface.

Electron Microscopy. Field-emission scanning electron microscopy (FE-SEM, Karl ZEISS JEOL) and transmission electron microscopy (TEM, FEI-Tecnai-G2) imaging analyses were used to understand the CFO surface morphology and particle size distribution. Analysis (Image-J software) of the micrographs was made to estimate the CFO NPs' size and distribution. The high magnification TEM imaging was done in order to quantify, more precisely, the role of OA concentration on the physical characteristics of CFO NPs. TEM images were obtained after placing a single drop (10 μL) of the aqueous solution onto a copper (Cu) grid coated with carbon film. The grid was allowed to dry in air at room temperature naturally. High-resolution images were acquired using FEI Titan XFEG 60−300 kV spherical aberration-corrected microscope. Energy dispersive X-ray spectrometry (EDS) was used for the compositional analysis of pristine NPs. The EDS measurements were performed in the respective electron microscope. For consistency and reliable information, the CFO NPs prepared on the Cu-grid for TEM analyses were employed for the EDS measurements.

Small Angle X-ray Scattering (SAXS). To further understand the morphology and particle size and their distribution characteristics, CFO samples were probed by SAXS for which the measurements were carried out using a Rigaku small angle goniometer mounted on rotating anode X-ray generator. In these measurements, scattered X-ray intensity $I(q)$ was recorded using a scintillation counter with pulse height analyzer by varying the scattering angle 2θ.[27] The intensities were corrected for sample absorption and smearing effects of collimating slits.[27] In SAXS, the mesoscopic density fluctuations in a material are represented by scattered intensity $I(q)$, where q is the scattering vector.[28] In the present case, the scattering occurs due to the density fluctuations arising from the basic spherical shell CFO NPs. The scattering profiles of all the samples were analyzed based on polydisperse spherical particle model under monodispersed approx-

DOI: 10.1021/acsanm.8b02009
ACS Appl. Nano Mater. 2019, 2, 1828−1843

imation.[29] For the correlated structures of CFO NPs, interparticle mass fractal structure factors were taken into consideration for each sample. The spherical shell form factor is parametrized with an inner radius R_2 and outer radius R_1 of particle. A more detailed account of fitting procedures and underlying theory of SAXS is presented in the Supporting Information.

X-ray Diffraction (XRD). D8-Advanced Bruker X-ray powder diffractometer was used to perform XRD measurements using Cu Kα radiation (λ = 1.5406 Å). Powder sample was scanned slowly over a 2θ range of 20−80° at a scanning rate of 4° min^{-1}. Rietveld refinement was employed to obtain detailed structural information on the CFO NPs. To generate theoretical XRD patterns, ICSD data with collection code 109044 were used.

Infrared and Raman Spectroscopy. To better understand the adsorption mechanism of the OA on the surface of CFO NPs, the Fourier transform infrared spectroscopic (FTIR) measurements were performed on pure OA and CFO NPs prepared with a variable OA concentration. The FTIR spectra of powder samples were recorded with the FTIR spectrometer (JASCO-6100) in the range of 400−4000 cm^{-1}. Nanoparticles were analyzed by dispersing powders in KBr as 1:4 ratios followed by grinding and prepared the pellets. In addition to FTIR measurements, Raman spectroscopic measurements were made to probe the chemical effects of OA and its concentration on the chemical bonding and local structure. Raman spectroscopic studies were performed on an InVia Micro RAMAN (Renishaw) spectrophotometer with 532 nm laser excitation. The recorded Raman spectra of all the samples were fitted by superposition of Lorentzian peak shape function.

X-ray Photoelectron Spectroscopy (XPS). Chemical composition analyses were made using X-ray photoelectron spectroscopy (XPS). Al Kα (1486.6 eV) X-ray source was employed for XPS measurements.

Magnetic Measurements. Magnetic measurements were performed using the Quantum Design (QD) Evercool II PPMS-6000. The magnetization hysteresis (M-H) loops were measured at 385 and 5 K by applying the magnetic field up to ±60 kOe. The temperature dependent magnetization, i.e., $M(T)$, was measured under an applied magnetic field of 100 Oe and over a temperature range from 10 to 395 K and zero-field-cooling (ZFC) and field-cooling (FC) conditions.

III. RESULTS AND DISCUSSION

A. Morphology, Crystallography, and Structural Chemistry. *Electron Microscopy.* The FE-SEM images shown in Figure S1 represent the morphology of the CFO NPs prepared with different OA concentrations. The images confirm that the particles are nanosized and spherical in shape. Agglomeration among the NPs increases slightly with increasing OA concentration. The high magnification TEM data provided, more precisely, insights into the role of OA content on the CFO NPs' size and morphology. The TEM data are presented in Figure 1. The particle sizes (D_{TEM}) obtained from TEM are ~10.83 ± 1.02 nm and ~6 ± 1.02 nm with the polydispersity indexes (σ) ~0.21 nm and ~0.29 nm for S1 and S2, respectively. As seen, the CFO NPs size decreases with increasing OA concentration. Note that the complexity of chemical solutions, i.e., slight changes in experimental conditions, can strongly influence the particle size and morphology.[30] In the present case, while the solvent, heating profile, reaction time, total concentration of precursors of ≅0.3 M were maintained constant, size reduction is noted for CFO NPs as a function of precursor-to-surfactant ratio. It has been observed that the NPs were self-assembled due to magnetic interaction and result into a bunch of NPs. Diffraction circles from (220), (311), (400), (511), (440), (531), and (444) crystal planes of CFO are noted in SAED data (Figure 2a−c). Also, the presence of lattice fringes with a spacing of 0.26, 0.48, and 0.47 nm, which correspond to the (220) and (400) crystal planes of CFO, is evident in HRTEM data (Figure 2d−f) of S1, S2, and S3 samples, respectively. These results indicate that the CFO NPs synthesized are highly crystalline, uniform, and randomly oriented and favorable to further probe the surface spins' influence on the magnetism. It should also be pointed out that the OA concentration effectively determines the NP size distribution and agglomeration. Thus, using the present approach, one can tune the nanoparticle size as per the targeted application, especially for utilization in field emission based electronic display and flexible electronic devices.

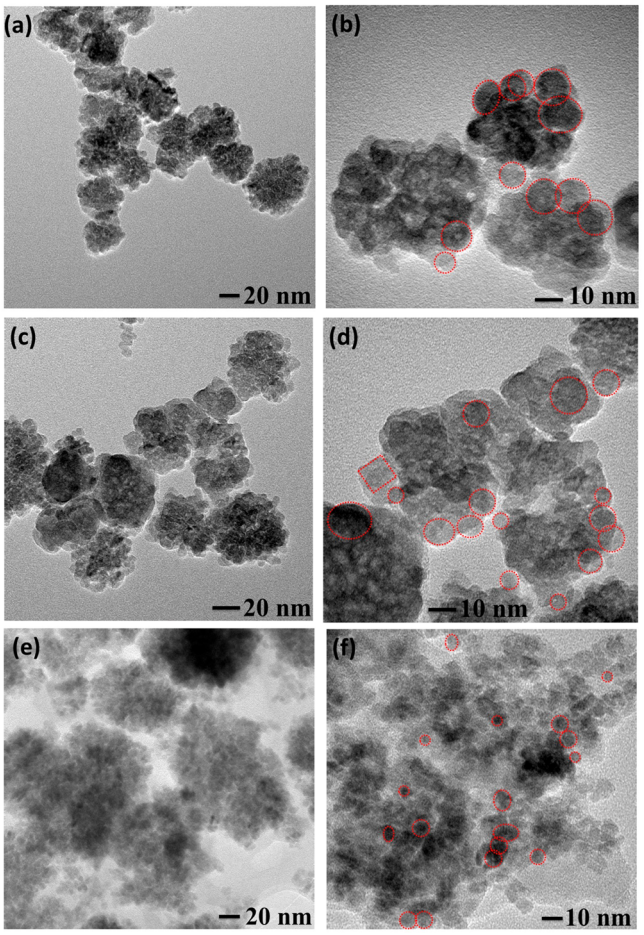

Figure 1. TEM images for S1 (a, b), S2, (c, d), and S3 (e, f) samples, respectively. Scale is 20 nm for parts a, c, e and 10 nm for parts b, d, and f.

Small Angle X-ray Scattering. The SAXS data are shown in Figure 3, where the scattering profiles are shown. The experimental data along with fitted curves are shown for all the samples, while the detailed fitting procedure/theory is outlined in Supporting Information. Table 1 summarizes the structural parameters obtained. The implications of variable OA content on the CFO physical properties, as derived from SAXS, can be summarized into two key points. (i) All the samples have two contributions: (a) basic spherical shell nanoparticles with mass fractal morphology and (b) inhomogeneity on a smaller length scale (~2 nm) which could be due to OA capping over the NPs. (ii) Average size of CFO NPs decreases with increasing OA concentration. Figure 4 shows the size distribution profiles, which are corroborating those results obtained from TEM. From this analysis, the

DOI: 10.1021/acsanm.8b02009
ACS Appl. Nano Mater. 2019, 2, 1828−1843

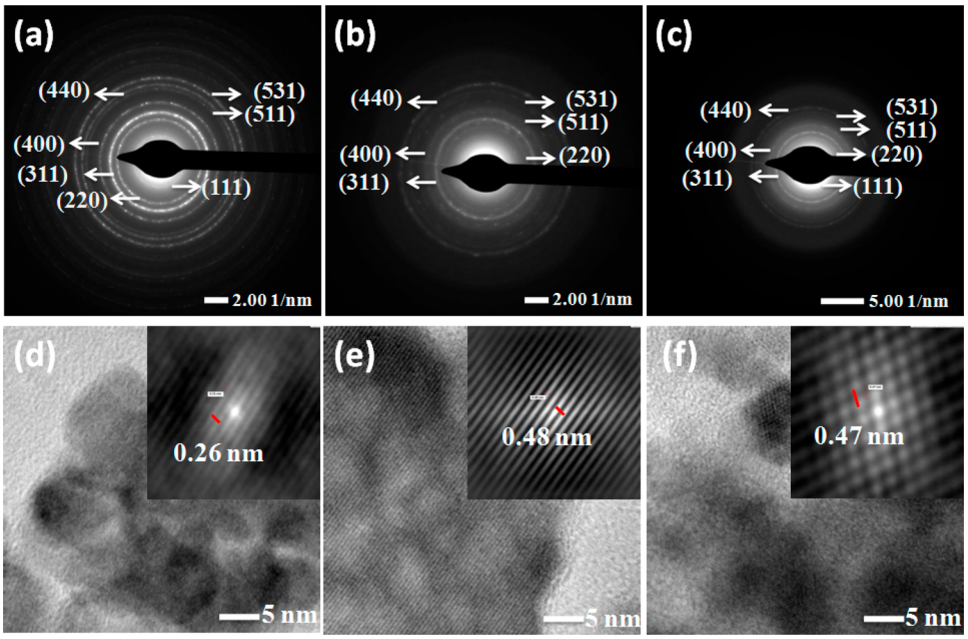

Figure 2. SAED pattern (a–c) and HRTEM images (d–f) for S1, S2, and S3 samples, respectively.

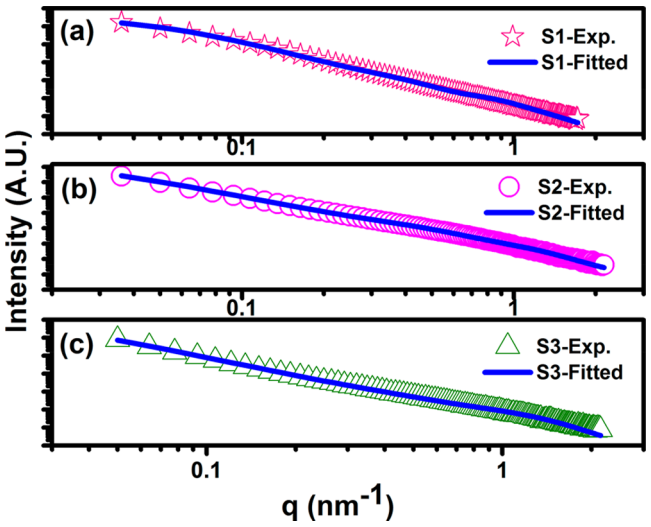

Figure 3. SAXS profile in double logarithmic scale for S1, S2, and S3 samples. Solid line represents the fit of model to the experimental curve.

Table 1. Structural Parameter Obtained from SAXS Data

samples parameters	S1	S2	S3
outer radius (R_1, nm)	6.32	4.02	3.59
inner radius (R_2, nm)	4.35	2.05	1.17
polydispersity index (σ, nm)	0.16	0.26	0.33
radius of the monomer (r_o, nm)	3.79	3.37	3.11
size of aggregate (x_i, nm)	20.53	44.92	51
fractal dimension (D)	2.99	2.83	2.81

average outer radius of NPs is found to be 6.32, 4.02, and 3.59 nm for S1, S2, and S3 samples, respectively. It is observed that the difference between outer and inner radius, i.e., ΔR, is found to be <2 nm for S1 and S2, which indicates the OA monolayer coating (OA length size of ∼0.97 nm) for S1 and S2 samples. On the other hand, ΔR > 2 nm noted for S3 sample implies the multilayer OA coating. This agrees well with thermal analysis where the weight loss was <20% for S1 and S2 samples, confirming the monolayer coating of OA. Multilayer surfactant coating occurs for S3 sample for which the weight loss is >20%. It is noteworthy that the size of the fractal aggregate and monomer radius also decreases with increasing concentration of OA.

The marginal differences in the trend of particle-size distribution, polydispersity index, and mean size as obtained from SAXS and TEM may be due their specific sensitivity and origin of the probing. It must be noted that SAXS provides structural information averaged over a wider region of the samples and gives the statistically averaged information whereas electron-microscopy-based techniques such FESEM and TEM provide direct but local information based on the region of interest or a selected smaller region. In this circumstance, it will be more consistent to believe or accept the structural information obtained via the applied scattering technique (i.e., SAXS data). As the crucial magnetic properties strongly depend on the structural parameters of the systems, it becomes more sensitive when dealing with the materials and systems at nanoscale dimensions. Overall, the structural and morphological analyses via TEM and SAXS strongly suggest or provide evidence that the particle size of CFO NPs decreases with increasing OA concentration. The energy dispersive X-ray spectrometry (EDS) analysis of the samples was employed to understand the chemical composition and homogeneity of the pristine CFO NPs. The EDS spectrum obtained for all the samples are shown in Figure S2. The results indicate the as-synthesized CFO NPs are chemically homogeneous without any impurities and/or contaminating elements from reagents. Furthermore, presence of C is expected due to the capping of OA ($CH_3-(CH_2)_7-CH=CH-(CH_2)_7-COOH$) on the surface of NPs.

X-ray Diffraction. The primary purpose of XRD analyses is to understand the effect of OA concentration on the crystal structure and the average crystallite size of CFO NPs. X-ray diffraction patterns (Figure 5) along with the Rietveld refinement indicate that all the samples are crystallized in the cubic structure in agreement with JCPDS card no. 22-1086

DOI: 10.1021/acsanm.8b02009
ACS Appl. Nano Mater. 2019, 2, 1828–1843

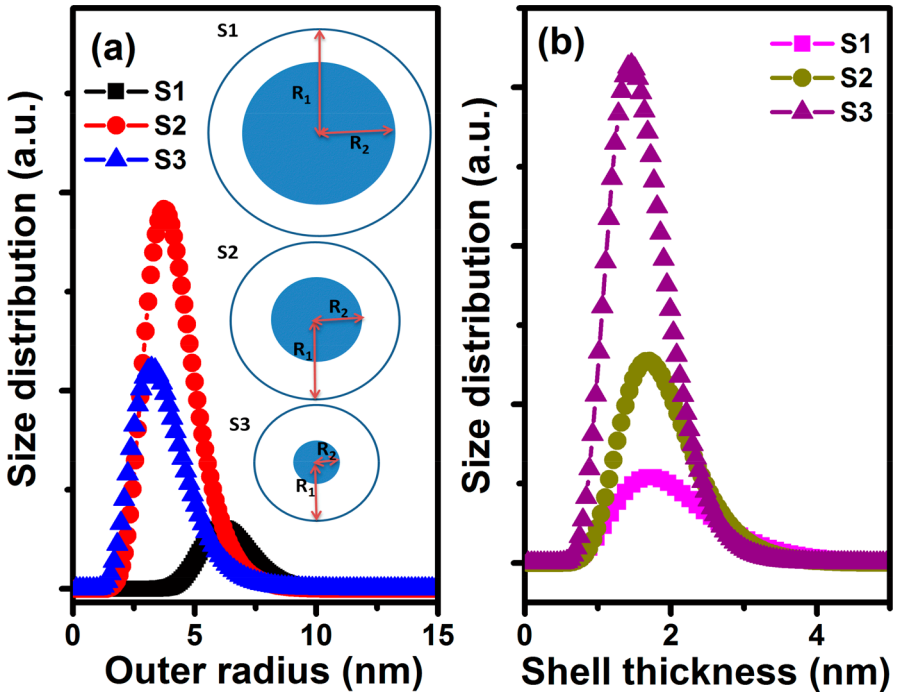

Figure 4. Size distribution obtained from SAXS profile for S1, S2, and S3 samples.

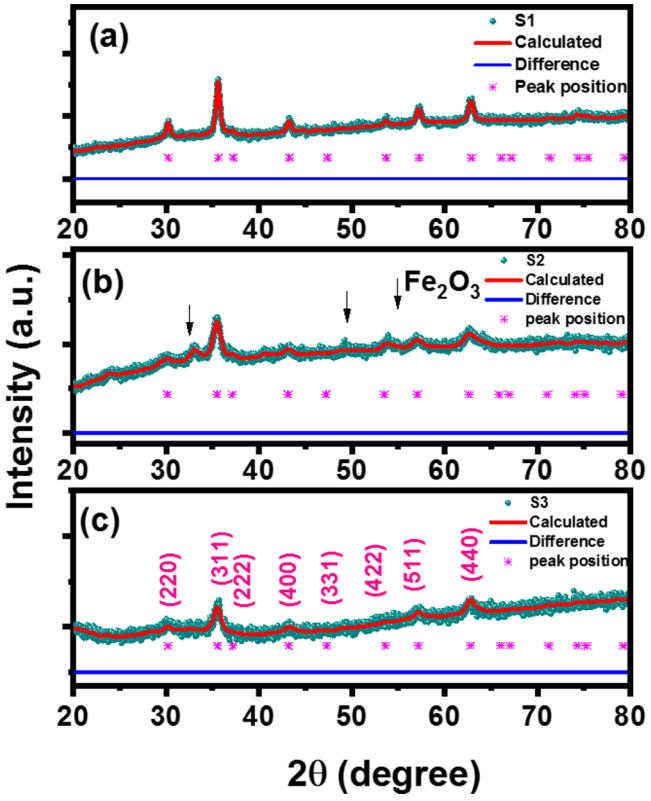

Figure 5. XRD data of CFO NPs. Rietveld refined XRD patterns along with experimental data are shown for (a) S1, (b) S2, and (c) S3 samples, respectively.

with a space group *Fd*3*m* (227) without any impurities except for S2. Sample S2 exhibits a weak peak of hematite, Fe_2O_3, phase at 2θ = 32.29° (JCPDS card no. 33-0664). The crystal structure parameters resulting from refinement procedure are listed in Table 2. With increasing OA concentration, the

Table 2. Structural Parameters Obtained from Rietveld Refinements of XRD Analysis

sample	goodness of fit (GoF) (χ^2)	crystallite size (nm) for (311) peak (±0.15)	lattice parameter (a, Å) (±0.015)	X-ray density ($d_{X\text{-ray}}$, g/cm^3)	volume of unit cell (V, nm ^{3})
S1	0.964	15.4	8.365	5.324	0.585
S2	1.07	8.94	8.393	5.271	0.591
S3	1.01	6.89	8.377	5.302	0.588

diffraction peaks become broader implying the average crystallite size reduction. The average crystallite size estimated from XRD data indicates a reduction from 15.4 to 6.89 nm which agrees with the other reports.[22] Thus, by varying the concentration of OA, one can tune the crystallite size of CFO NPs. Furthermore, the lattice constants for S1 and S3 samples are found to be smaller compared to bulk CFO (8.391 Å). Such lower values for NPs compared to bulk may be predominantly due to reduced dimensionality size-effects, which also include surface dipole interactions, surface tension, and cation charge distribution,[1,31] whereas for S2 sample, the lattice constant value is slightly larger than that of the bulk CFO which may be due to the presence of hematite phase. Overall, it is inferred that the crystallite size decreases while lattice parameters vary due to change in OA concentration. From the structural analysis, CFO NP size decreases; however, agglomeration becomes dominant at higher OA concentration (S3). Thus, fundamentally, OA addition controls the nucleation, growth, and size of CFO NPs. Variation in crystallographic parameters was also noted in doped and size-controlled CFO.[1] In ferrites, the lattice constant is usually affected by the cationic stoichiometry. However, in the present case, OA coating has not affected the cationic balance (confirmed by XPS) but affects the particle size and the average crystallite size as evidenced in TEM, SAXS, and XRD analyses. Therefore, lattice parameter variation in CFO NPs

DOI: 10.1021/acsanm.8b02009
ACS Appl. Nano Mater. 2019, 2, 1828−1843

Table 3. Bond Angle and Bond Length Extracted from Rietveld Refinement for the Samples

	bond angle (deg)				bond length (Å)		
	S1	S2	S3		S1	S2	S3
Co1−O−Fe2	125.26	125.25	124.26	d_{12} = Co1−O	2.091	2.098	2.094
				d_{23} = O−Fe2	1.811	1.8172	1.814
				d_{13} = Co1−Fe2	3.468	3.478	3.471
O−Fe2−O	109.47	109.47	109.47	d_{12} = O−Fe2	1.811	1.817	1.814
				d_{23} = Fe2−O	1.811	1.817	1.814
				d_{13}= O−O	2.957	2.967	2.962
O−Co1−O	90	90	90	d_{12} = O−Co1	2.091	2.098	2.094
				d_{23} = Co1−O	2.091	2.098	2.094
				d_{13} = O−O	2.957	2.967	2.962
				Co1−Co1	2.957	2.967	2.962
				Co1−Fe2	3.468	3.478	3.473

may be following a different mechanism. Note that the occupancy and Wyckoff positions of Co^{2+} and Fe^{3+} cations are nearly same for all the samples at tetrahedral as well as octahedral sites (Table S1). Moreover, different occupancy was observed for oxygen anion for all the samples. Therefore, it appears that OA established the chemical coordination with oxygen in the lattice with the covalent bond (from FTIR) being the origin. As a result, overall charge compensation of CFO can become disturbed. Additionally, lattice defects may be generated. All these factors may contribute to variation in lattice parameters. From Table 3, it can be seen that the bond lengths observed at tetrahedral site and octahedral site, i.e., O−Fe2, O−Co1 bond lengths, and intercation distances, i.e., Co1−Co1, Co1−Fe2, slightly change with OA concentration. Simultaneously, it is evident from the bond angles observed at tetrahedral and octahedral sites that the S1, S2, and S3 samples are stabilized in the cubic structure with almost no local distortion at the tetrahedral and octahedral sites. The O−Fe2−O and O−Co2−O angles exactly match with an ideal spinel value of 109.47° for all the samples. In addition, the O−Co1−O and O−Fe1−O bond angles are found to be in agreement with the ideal value of 90°. Similarly, in agreement with ideal value, the angle of Co1−O−Co2, Fe1−O−Co2, Co1−O−Fe2, and Fe1−O−Fe2 bonds is observed to be 125.26° for all the samples. Therefore, (i) absence of local distortion at tetrahedral and octahedral sites and (ii) decrease in size from 15 to 6.89 nm strongly support the major role of oxygen and covalent bond formation of OA with CFO NPs. Different values of oxygen occupancy observed from diffraction data also support the observations made for all the samples.

B. Thermogravimetric (TGA) Analysis. The TGA data (Figure 6) reveal distinct four- and three-step weight loss for S2 and (S1, S3) samples, respectively. Initial weight loss (~50−100 °C range) of 1.37%, 2.86%, and 1.24%, observed for S1, S2, and S3, corresponds to chemical desorption of moisture and volatile components. S1 and S3 samples exhibit the second weight loss of 4.69% and 13.93% in the temperature range of 92−374 °C and 90−465 °C, respectively. Since the decomposition temperature of OA is 360 °C, this weight loss must be due to the separation of functional groups (COOH) from surfactant layer. The third weight loss values of 1.43% and 32.43% in the temperature range of 374−900 °C and 465−690 °C were mainly from CO and CO_2 effluents from the S1 and S3, respectively. On the other hand, S2 exhibits the second and third weight loss of 2.76% and 3.68% due to the breaking of weakly and well-bound functional groups (COOH) from surfactant molecules. And the fourth

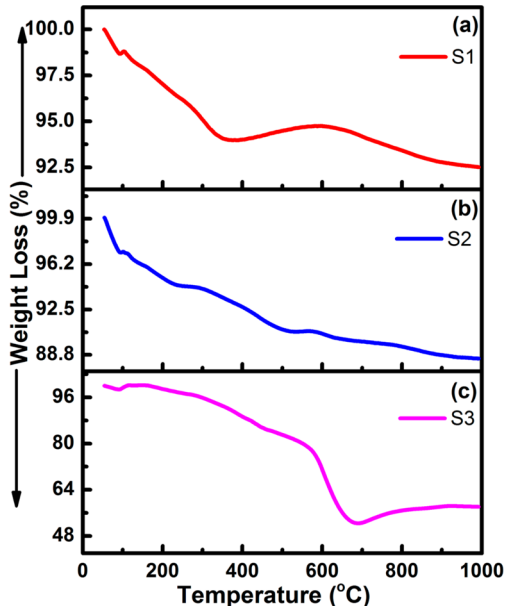

Figure 6. Thermogravimetric curve (under air atmosphere) for (a) S1, (b) S2, and (c) S3 samples.

weight loss of 2.2% is observed in 536−900 °C range. Overall, the total weight loss was observed to be 7.49%, 11.5%, and 47.11% for S1, S2, and S3, respectively. The thermal behavior of samples depends on several factors, namely, structure, homogeneity, composition, etc. Usually, a decrease in the particle size leads to a faster release of decomposition products, i.e., faster weight loss. The particle size reduction increases the surface area, as observed from calculation, leading to more uptake of water molecules and their release during heating. It has been reported that monolayer coating of surfactant is present when weight loss is <20% and several layers of surfactant are present when weight loss is >20%.[32,33] Thus, surfactant forming a monolayer on individual CFO NPs is evident for S1 and S2, whereas several surfactant layers are for S3, as the weight loss is >20%. For spherical NPs of diameter d, close-packed surfactant monolayer OA molecules occupy surface area "a", and the surface area per particle is $\sim\pi d^2$. Then, total number of particles is $[(100 - W)/\rho](\pi d^3/6)$, where "$W$" is the weight of surfactant in percentage and "ρ" is the density of particle. If M is the surfactant molecular weight, the total number of surfactant molecules is WN_0/M, where, N_0 is Avogadro number. Therefore, the surface area "a" occupied by OA molecules is given by

DOI: 10.1021/acsanm.8b02009
ACS Appl. Nano Mater. 2019, 2, 1828−1843

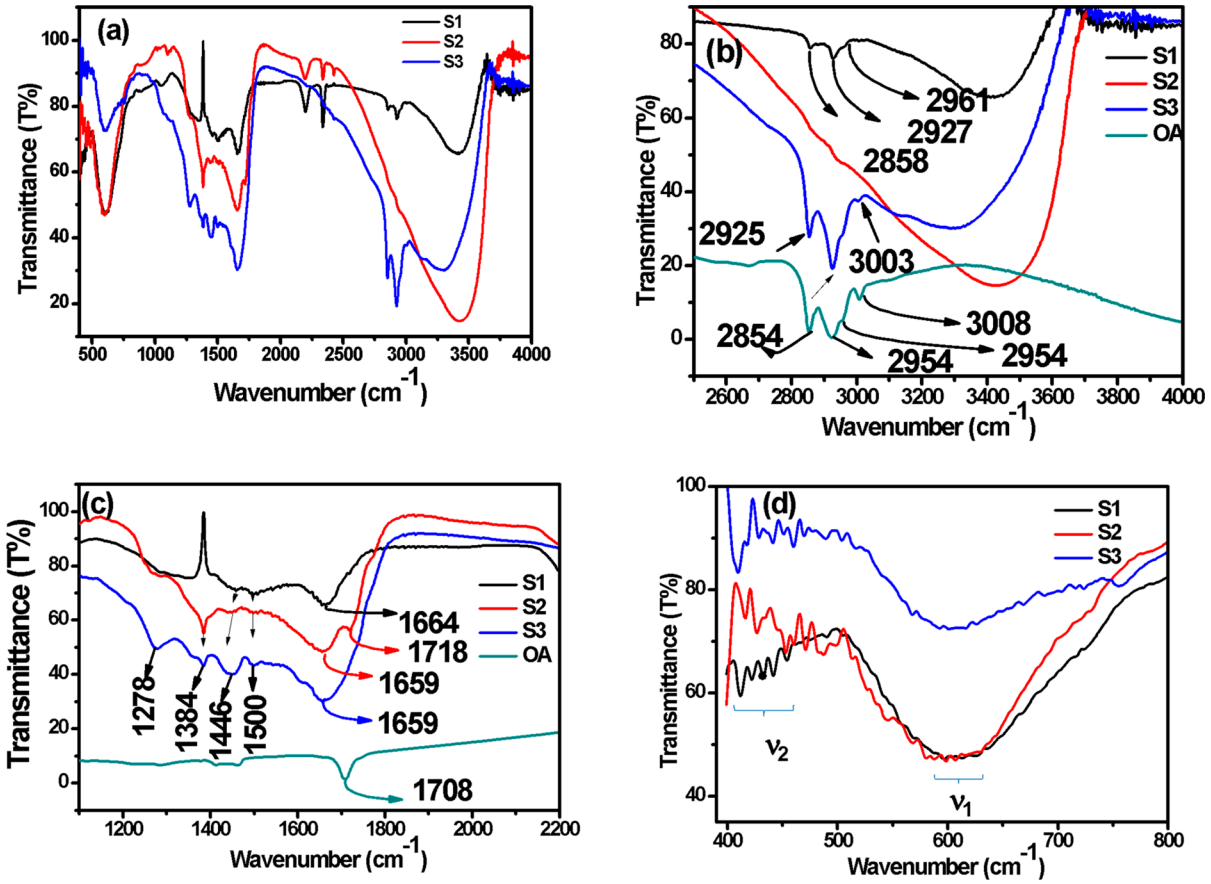

Figure 7. FTIR spectra for S1, S2, and S3 samples (a) for 400−4000 cm^{-1} and, for clarity, the magnified data (b) from 2500 to 4000 cm^{-1}, (c) from 1100 to 2200 cm^{-1} that show asymmetric and symmetric $-COO^-$ stretching bands, (d) from 400 to 800 cm^{-1} which confirm the capping of OA and pure phase formation of CFO NPs.

$$a = \frac{6(100 - W)M}{N_0 d\rho W} \quad (1)$$

Thus, the surface area of OA molecule on CFO is 0.516 nm^2, 0.501 nm^2, and 0.081 nm^2 for S1, S2, and S3, respectively.[32,33] Furthermore, by use of weight loss, the number of OA molecules per particle can be estimated as

$$N = \frac{WN_0\rho\frac{4}{3}\pi R^3 \times 10^{-23}}{M} \quad (2)$$

where N is the number of surfactant molecules (ligands) per particle, W is the weight loss in percent (%), N_0 is Avogadro's number, ρ is the density of NPs, R is the average radius of CFO NPs (obtained from SAXS analysis), and M is the molecular weight of OA (282.47 g/mol). The number of OA ligands per particle is ∼899, 351, and 1041 for S1, S2, and S3, respectively.[24,30]

C. Chemical Bonding, Stability, and Surface Chemistry. *Fourier Transform Infrared Spectroscopy.* The FTIR spectra of the samples are shown in Figure 7. Identification of peaks and mode assignment was made in accordance with the literature.[19,34,35] Vibrational modes observed for pure OA and OA coated CFO are presented in Supporting Information (Tables S2 and S3). A detailed description of FTIR spectra of pure OA is also presented in Supporting Information. Figure 7a presents the FTIR spectra (400−4000 cm^{-1}) for S1, S2, and S3. From magnified data in the range of 2500−4000 cm^{-1}(Figure 7b), it has been observed that the S1, S2, and S3 samples exhibit a broad peak at 3420 cm^{-1} and a broad peak at 3301 cm^{-1}, which are due to stretching vibrations of hydroxyl groups likely originating from sample moisture.[36] A weak peak at 3003 cm^{-1}, which is due to C−H stretching of the ═C−H group, can be noted only for S3 sample, while it is absent for S1 and S2 samples. Furthermore, the $-CH_2-$ scissoring band is found to be at 1458 cm^{-1} for S1 sample, whereas this band is shifted to 1446 cm^{-1} for S2 and S3 samples. Furthermore, $-CH_2-$ scissoring band becomes broader and intense for S3 compared to S1 and S2 samples. The absorption band positioned at 1384 cm^{-1}, which is clearly noted for S2 and S3 samples, is assigned to the vibration of double covalent bond in −CH═CH−. The asymmetric and symmetric stretching of a $-CH_2-$ group is positioned at (2927, 2925) cm^{-1} and (2858, 2854) cm^{-1}, respectively. These IR bands are more intense for samples S1 and S3 compared to S2. Meanwhile, asymmetric stretching of a $-CH_3$ group appears as a weak shoulder at 2961 cm^{-1} for S1 and S2 (Figure 7b). It is essential to mention that the two new peaks found at 1664 (for S1 only) and 1500 cm^{-1} (for S1, S2, and S3) (Figure 7c) are typical and ascribed to the asymmetric and symmetric stretching, respectively, of a $-COO^-$ group. According to literature, confirmation for the capping of OA is revealed by the absence of −C═O stretching bond of the carboxyl group (OA) and the presence of two characteristic bands of asymmetric and symmetric $-COO^-$ stretching bands.[36] Thus, in the present study, it is evident that the −C═O stretching band of the carboxyl group, which is present at 1708

DOI: 10.1021/acsanm.8b02009
ACS Appl. Nano Mater. 2019, 2, 1828−1843

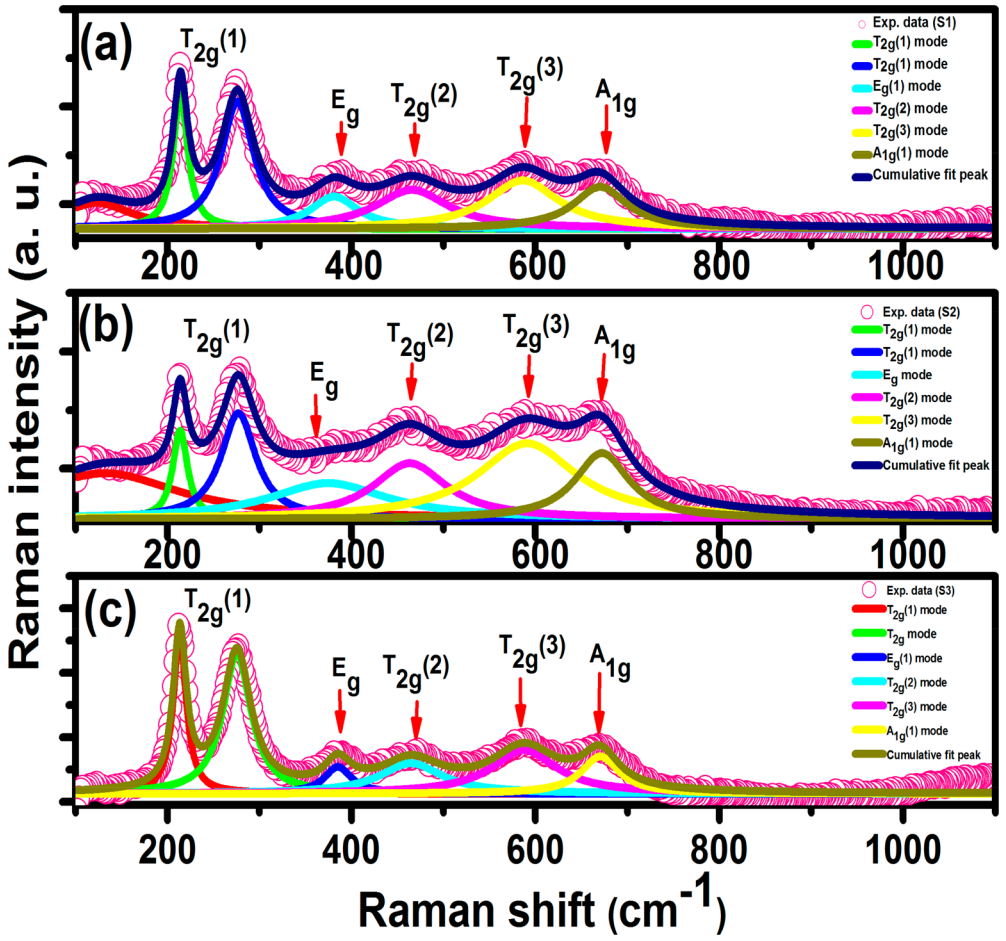

Figure 8. Raman spectrum for (a) S1, (b) S2, and (c) S3 samples, where the experimental data, Raman active modes fitted with cumulative fit are shown.

cm^{-1} for pure OA (Figure S3), is fully absent in the spectra for S1, S2. and S3 samples (Figure 7c). However, the asymmetric stretching of a $-COO^-$ group shifts to 1659 cm^{-1} for S2 and S3 samples. Also, for all the samples, the asymmetric stretching of a $-COO^-$ group is more intense compared to symmetric stretching of a $-COO^-$ group. The asymmetric stretching of a $-COO^-$ group is found to be broader and more intense for S3 compared to S1 and S2 samples. Also, with increasing OA concentration, broadening of the asymmetric stretching of a $-COO^-$ group increases. The difference in the average crystallite size accounts for this observation; enough space available to ligands to orient to stable conformation in larger nanocrystals is not readily possible in smaller sized nanocrystals. In addition, more surface related defects and thus faster vibrational relaxation occur in smaller size nanocrystals. Interestingly, S3 sample exhibits weak shoulder absorption band at 1608 cm^{-1}. In addition, a weak peak at 1718 cm^{-1} suggests the physically absorbed OA for S2 only. Overall, the absence of (−COOH) characteristic peak suggests the formation of OA monolayer on the surface of CFO NPs and we assume that the interaction of OA for S2 is poor compared to S1 and S3. Thus, the absence of signature peak for the carbonyl group and a decrease in intensity of the broad signal with increasing OA concentration are the highlights of IR spectra.

Furthermore, wavenumber separation (Δ) between the asymmetric and symmetric ($-COO^-$) stretching bands dictates the type of interaction present between the carboxylate and metal atoms on the surface. The four types of interactions are monodentate, bridging bidentate, chelating bidentate, and ionic interaction. For monodentate interaction, Δ is largest (~200−320 cm^{-1}) while the smallest Δ (<110 cm^{-1}) corresponds to the chelating bidentate. Bridging bidentate interaction is characterized by the intermediate or medium range Δ (~110−200 cm^{-1}). The Δ values were 164, 159 cm^{-1} for S1, (S2 and S3) samples; thus, the characteristic bridging bidentate interaction where both the oxygen atoms of OA form a covalent bond with the two different metal atoms on the surface is evident. Furthermore, the IR spectra exhibit two more absorption bands below 700 cm^{-1} as expected for ferrite NPs (Figure 7d). First absorption band (ν_1) is observed at 609, 597, and 599 cm^{-1}, and second band (ν_2) is positioned at (412, 422, 433, 442, and 454 cm^{-1}), (416, 427, 453, 460, and 470 cm^{-1}), and (410, 418, 429, and 442 cm^{-1}) for S1, S2, and S3 samples, respectively. The second band (ν_2) could not be seen clearly since it is beyond the detection limit of our FTIR equipment (<400 cm^{-1}). Thus, the formation of single phase spinel structure having two sublattices, tetrahedral (A) site and octahedral (B) site, is confirmed by the absorption bands observed in the limit. Stretching vibrations of the tetrahedral metal (Fe^{3+})−oxygen bond causes ν_1 while ν_2 is due to the octahedral metal i.e., Co^{2+}−oxygen and F^{+3}−oxygen bond vibrations at octahedral sites. In the FTIR spectra recorded, the position of the tetrahedral peak is at higher region compared to

DOI: 10.1021/acsanm.8b02009
ACS Appl. Nano Mater. 2019, 2, 1828−1843

Table 4. Raman Vibrational Data along with the Assigned Modes for S1, S2, and S3 Samples

sample	peak position (cm^{-1})	fwhm (cm^{-1})	area (cm^{-2})	height (cm^{-1})	Raman mode	assigned polyhedra
S1	214.09	19.25	42020	1389.60	$T_{2g}(1)$	CoO_6 or FeO_6 octahedra
	276.12	42.91	88210	1308.67	$T_{2g}(1)$	
	381.24	63.54	33276	333.37	E_g	
	465.66	96.96	61039	400.75	$T_{2g}(2)$	
	586.26	94.40	73721.57	497.18	$T_{2g}(3)$	
	670.54	70.78	48109.69	432.69	A_g	FeO_4 tetrahedra
S2	213.76	19.58	23314.36	757.91	$T_{2g}(1)$	CoO_6 or FeO_6 octahedra
	277.04	46.17	65617.96	904.77	$T_{2g}(1)$	
	374.96	157.97	76088.74	306.62	E_g	
	463.51	98	73424.75	476.97	$T_{2g}(2)$	
	590.93	131.54	133453.44	645.87	$T_{2g}(3)$	
	672.47	71.71	63574.23	564.31	A_g	FeO_4 tetrahedra
S3	213.27	17.27	133427.09	4918.09	$T_{2g}(1)$	CoO_6 or FeO_6 octahedra
	275.43	37.22	254592.46	4354.17	$T_{2g}(1)$	
	385.31	36.03	47552.41	840.01	E_g	
	464.71	83.15	123774.48	947.63	$T_{2g}(2)$	
	587.65	86.80	185414.32	1359.75	$T_{2g}(3)$	
	670.48	50.46	91834.22	1158.47	A_g	FeO_4 tetrahedra

octahedral peak. Due to shorter bond length of the Fe−O bond at the tetrahedral lattice (compared to octahedral lattice, Table 3), more energy is required for the vibration. Therefore, the ν_1 and ν_2 intensity difference arises to the changes in bond lengths within octahedral versus tetrahedral site. In addition, minor splitting of the octahedral band observed near ν_2 is attributed to the "'Jahn−Tellar"' distortion, which is produced by Fe(II) ions causing the local deformation in the crystal field potential with a result of the absorption band splitting.[37,38]

Raman Spectroscopy. The chemical effects of OA and its concentration on the CFO NPs were further confirmed by the Raman spectroscopic data, which are presented in Figure 8 and Table 4. The deconvoluted Raman spectra for all major peaks of the samples along with their fits are presented in Figure 8, while parameters derived are summarized in Table 4. High quality cubic symmetry of CFO is further confirmed by the well-defined peaks observed in Raman spectra. For CFO with an inverse cubic spinel structure (space group $Fd3m$ (O_h^7)), group theory predicts five Raman active modes, i.e., $A_{1g} + E_g + 3T_{2g}$. Thus, phonon mode assignment was carried out in accordance with the literature.[1] Raman peaks at 671, 672, and 670 cm^{-1} for S1, S2, and S3 samples, respectively, represent the A_{1g} mode, which is ascribed to the symmetric stretching of oxygen with respect to metal ion in tetrahedral void. For S1, S2, and S3 samples, respectively, the E_g, $T_{2g}(2)$, and $T_{2g}(3)$ modes are reflected in the peaks located at E_g of 381, 375, and 385 cm^{-1}, $T_{2g}(2)$ of 466, 464, and 465 cm^{-1}, and $T_{2g}(3)$ of 586, 591, and 588 cm^{-1}. Principally, E_g and $3T_{2g}$ phonon modes that appear at <600 cm^{-1} are attributed to the symmetric and antisymmetric bending of oxygen ion in M−O bond at octahedral voids (BO_6). Furthermore, in the present case, $T_{2g}(1)$ mode is found to be at 276, 277, and 275 cm^{-1} along with one more additional peak which seems to be doublet peak for S1, S2, and S3, respectively. The component at ∼214 cm^{-1} is ascribed to the T_{2g} mode of Fe_3O_4 NPs.[39] The weak shoulder component, which is unassigned and located at 123 and 132 cm^{-1} for S1 and S2 samples, is attributed to defect, surface disorder, or oxidation of metal cations.[40] All the Raman modes are symmetric in nature; also, the modes experience a shift toward lower wavenumber (Table 4) with decreasing crystallite size from ∼15.4 to 8.94 nm for S1 and S2 samples. Crystalline disorder and grain boundaries, which are common in nanomaterials, account for such peak shift toward lower wavenumber. Full width at half-maximum (fwhm) is another important characteristic parameter of Raman signal. In the present study, it is observed that broadening is more intense for the S2 and S3 compared to S1. The peak broadening and shift (lower wavenumber), which are typical in polycrystalline materials, occur due to confinement of optical phonons in a nanocrystallites.[41,42] Furthermore, A_{1g}, $T_{2g}(3)$, and E_g (for S3 only) modes represent the blue shift for S2 and S3 samples. Due to covalent bonding with the metal ions on the surface, the OA capping layer may create lattice strain, which induces blue shift. Importantly, blue shift is more dominant for S3 compared to the S2 sample as the concentration of OA is higher (0.1 M) for S3 sample compared to S2. Evidently, compared to the rest of octahedral and tetrahedral Raman active modes, the $T_{2g}(1)$ mode is more intense. This may be due to increased magnetic ordering at octahedral site. However, while magnetic ordering alone is not the principal cause, Raman mode is affected by several other factors such as crystalline disorder, defect density, etc.[43]

X-ray Photoelectron Spectroscopy. The XPS data of CFO NPs are shown in Figure 9 and Figure S4 (Supporting Information). The survey scans and core-level XPS data are shown. The XPS data of the S1, S2, and S3 samples (Figures 9 and S4) exhibit O 1s, Fe 2p, Co 2p, and C 1s peaks and, thus, confirm the existence of the respective elements as expected. For S1 sample, the XPS of Fe 2p is presented in Figure 9b. The binding energy (BE) position of Fe 2p components, ΔE of Fe $2p_{3/2}$ (712.51 eV) and $2p_{1/2}$ (725.91 eV), and the presence of corresponding shakeup satellites at 719.9 and 734.49 eV, respectively, characterize the Fe chemical valence as +3.[44,45] Moreover, the BE for metallic state and Fe^{2+} is expected to be around 707 and 709.9 eV, respectively, and could not be detected in any of the samples. This observation rules out the possibility of lower valence of Fe.[46] For cobalt, Co^{2+} states are evident by the presence of characteristic 2p peaks at 782.96 and 797.87 eV and with their respective satellite components at 787.97 and 804.95 eV.[47,48] For all the samples, the O 1s peak is located at BE of ∼523.49 eV, which characterizes the O^{2-} ions in CFO.[49] However, XPS of S1 sample indicates a

DOI: 10.1021/acsanm.8b02009
ACS Appl. Nano Mater. 2019, 2, 1828−1843

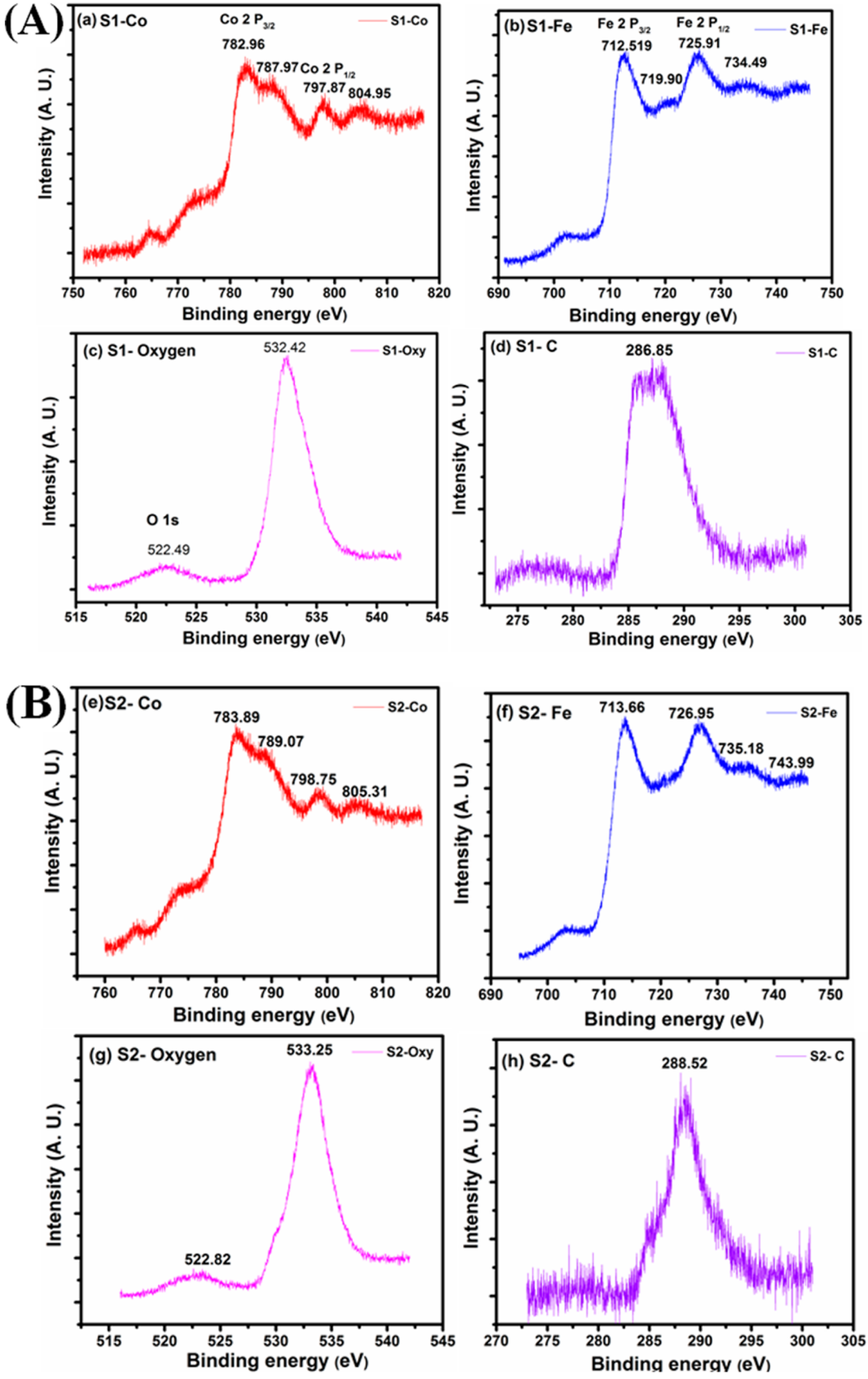

Figure 9. continued

DOI: 10.1021/acsanm.8b02009
ACS Appl. Nano Mater. 2019, 2, 1828−1843

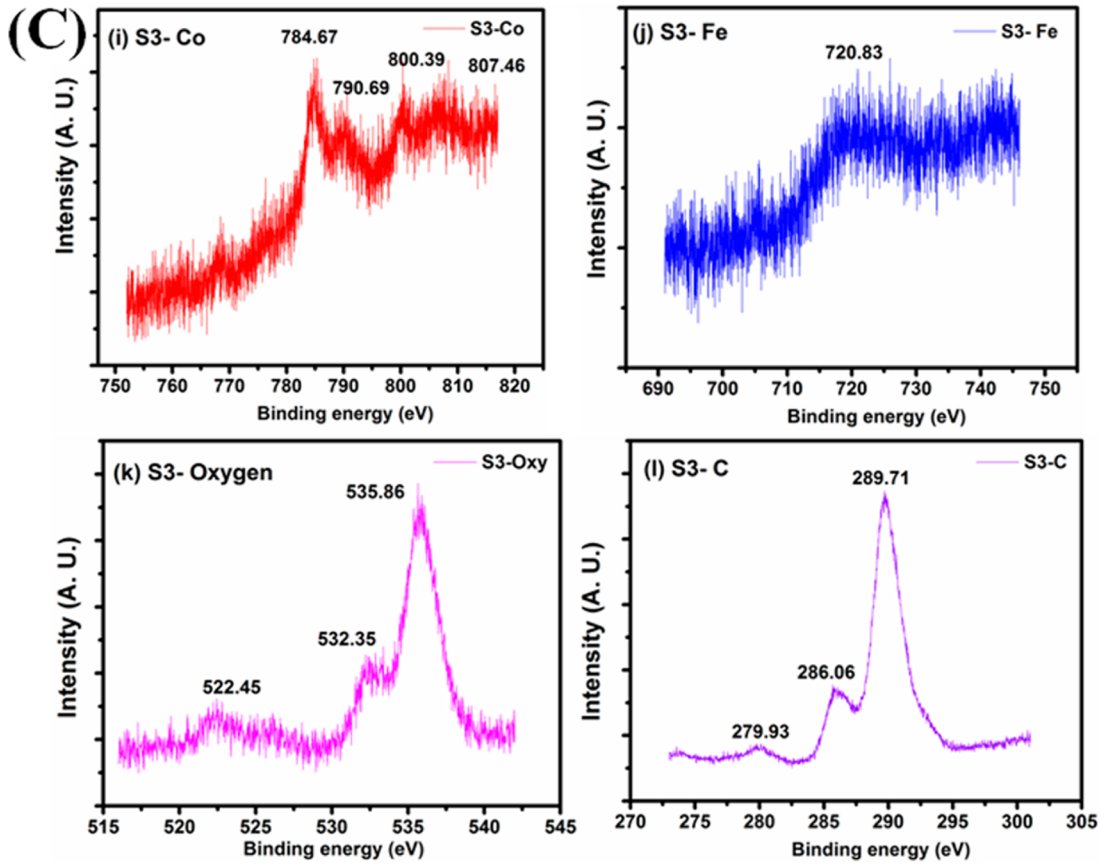

Figure 9. XPS spectra displaying the binding energy and chemical states of (A) S1, (B) S2, and (C) S3 samples where Co 2p, Fe 2p, O 1s, and C for S1 (a–d), S2 (e–h), and S3 (i–l) are shown for all the samples.

peak at BE of ∼532.42 eV, which is due to the $-COO^-$ carboxylate groups.[50,51] Corroborating with IR analyses, the carboxylate component in XPS validates the OA molecules bonded to the CFO NPs in bidentate form.[52] However, in CFO NPs, the minor contribution at BE of ∼532.1 eV is often formally described as O species, where oxygen is bonded to the surface and near-surface defect sites.[49] Furthermore, in all the samples, we could verify the presence of OA capping on the surface of the NPs by the presence of C peak which normally originates at 285 eV. However, it must be emphasized that the carbon peak in the XPS spectra may also be due to adventitious carbon from exposure of the samples to air following synthesis, before being placed in the XPS system. Therefore, while C 1s peak in XPS alone cannot provide more definite information, the presence of OA capping on the surface of the CFO NPs is validated more directly from FTIR results, which corroborate with XPS to some extent. Remarkably, with an increase in OA concentration, the peak position value of Co^{2+}, Fe^{3+}, O, and C is shifted toward the higher binding energy from S1, S2 to S3, respectively. As the S3 sample exhibits multilayer coating of OA, the poor signal is originated for Fe^{3+} and strong signal is observed for C, compared to S1 and S2 samples.

D. Magnetic Properties. The data shown in Figure 10a indicate that the irreversibility between ZFC and FC curves start well above 395 K; thus, overcoming of superparamagnetic limit in all the samples is at >395 K. Moreover, with decreasing temperature, it is seen that the bifurcation between the values of FC and ZFC magnetization increases which is indicative of high anisotropic behavior. For S1 and S3, at low temperatures, negative magnetization is measured at 100 Oe in ZFC condition. The negative magnetization is also reported in the literature.[53−55] However, a number of reasons such as structural phase transition, change in sign of f–d exchange interaction, spin reorientation, and negative coupling between interactions were considered.[55] The negative value of magnetization may be due to remnant magnetization, which is not compensated by 100 Oe field. Spectroscopic analyses indicate that the OA is well bonded for S1 and S3. Moreover, at lower temperature, in ZFC condition, the OA capped magnetic grains are restrained and do not respond to the applied magnetic field due to OA diamagnetic susceptibility.[56] With increasing temperature, for all the samples, the ZFC magnetization value remains constant up to ∼150 K and then increases to approach the FC value. CFO with different compositions and other ferrimagnetic samples were also reported to exhibit similar behavior.[57] Furthermore, a substantial change in the slope of ZFC magnetization (M_{ZFC}) curve noted near 200−316 K is more dominant for S2 and S3 samples. This behavior may be ascribed to charge ordering and metal–insulator transition.[58,59] The M_{ZFC} value increases with temperature, then attains the maximum (T_{max}) value at 384.9 K. Increased volume anisotropy and interparticle interaction account for T_{max} shift to higher temperatures.[15] To a first approximation, $T_{max} = AT_B$, where T_B is the blocking temperature and constant "A" takes values between 1 and 2.73. T_B was estimated to be ∼395 K; large anisotropy of CFO may be the reason for this relatively larger T_B. Clearly, all the OA coated CFO NPs exhibit the superparamagnetic character above 395 K. Presence of a frustrated surface spin layer can

DOI: 10.1021/acsanm.8b02009
ACS Appl. Nano Mater. 2019, 2, 1828−1843

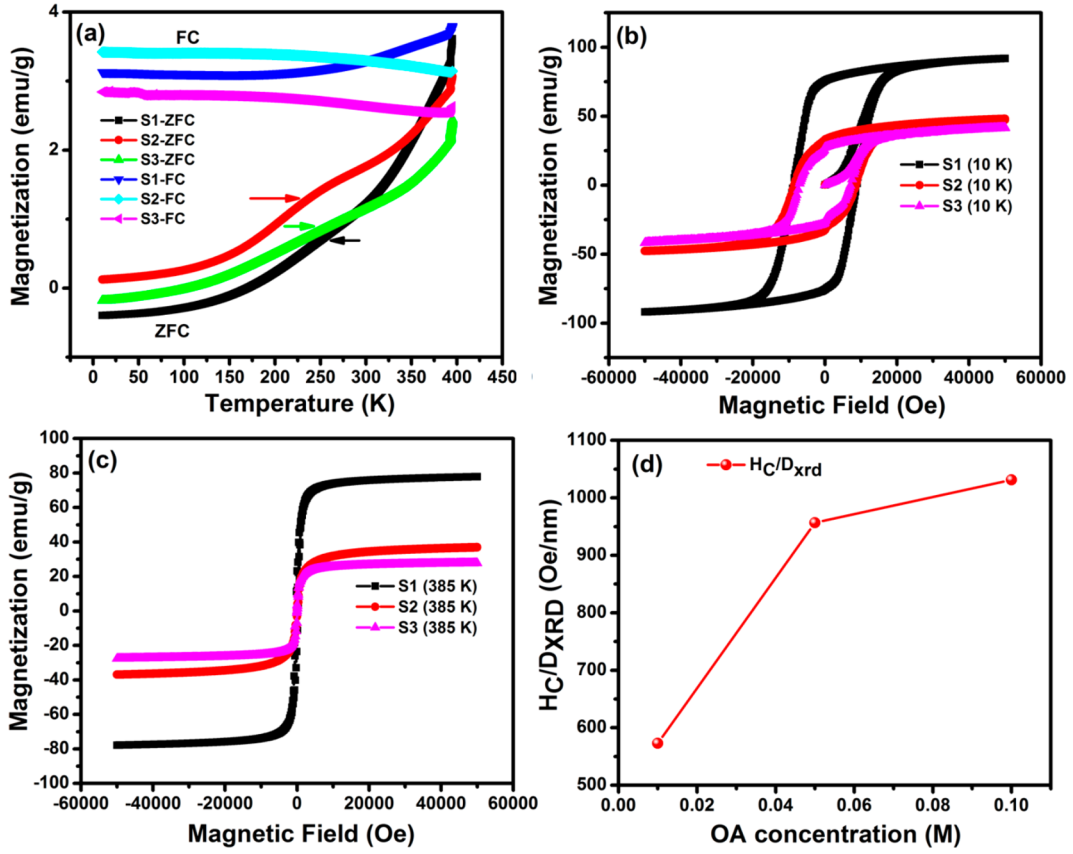

Figure 10. ZFC−FC curve measured at 100 Oe (a), M-H loops measured at 10 K (b) and at 385 K (c), and H_C/D_{XRD} versus OA concentration (d) plots for S1, S2, and S3 samples.

Table 5. Magnetic Parameters Obtained for CFO NPs

sample	temp (K)	M_S (emu/g)	M_S (μ_B/F.U.)	M_r (emu/g)	M_r/MS	H_C (Oe)	H_{ex} (Oe)	K_E (erg/cm^3)	H_{dip} (Oe)
S1	10	91.88	3.859	75.66	0.82	8823.36	39.345	6.74×10^6	49.56
	385	77.85	3.270	19.73	0.25	261.54	9.045	1.69×10^5	1672.14
S2	10	47.94	2.015	32.79	0.68	8551.52	25.735	3.38×10^6	186.69
	385	36.97	1.553	2.73	0.074	98.07	24.78	2.99×10^4	16279.23
S3	10	41.80	1.756	27.1	0.58	7106.17	−12.41	2.46×10^6	294.96
	385	27.70	1.164	3.14	0.11	63.19	36.24	1.45×10^4	33170.23

strongly contribute to the decrease of remnant magnetization ∼2.73 emu/g and 3.14 emu/g for S2 and S3 at 385 K.

Furthermore, for S1, the FC magnetization (M_{FC}) is observed to decrease initially with decreasing temperature from 395 to 168 K corresponding to noninteracting regions and then exhibits temperature independent behavior. In contrast, for S2 and S3, the M_{FC} increases with decreasing temperature from 395 to 130 K and then shows temperature independent behavior. Such inverse M_{FC} temperature trend, as noted for CFO nanotubes,[60] may be correlated to the larger magnetocrystalline anisotropy of CFO. Furthermore, saturated behavior observed for S1 and (S2, S3) below 168 and 130 K could be a result of finite-size interaction effects, which arise from dipolar and interparticle coupling interactions.[2]

Figure 10b,c shows the magnetization (M-H) loops measured at 10 and 385 K for variable applied magnetic fields up to ±50 kOe. The magnetic parameters obtained are listed in Table 5. For S1 sample, the M_S value is slightly high (91.88 emu/g or 3.859 μ_B/F.U.) compared to the theoretical value for an ideal inverse CFO structure (3 μ_B/F.U.), the bulk counterpart (80 emu/g), and CFO NPs.[2] Here, an increment in M_S value for S1 may be attributed to the slightly nonstoichiometric cation distribution (Fe^{3+}, Co^{2+}) among the octahedral and tetrahedral sites as compared to ideal spinel structure $[Fe^{3+}]\{Co^{2+}Fe^{3+}\}O^{2-}$ as predicted by the XRD refinement data. Increasing OA decreases M_S value due to the presence of surfactant molecule, smaller magnetic cores, and surface disorder or spin canting at the NP surface.[2,20] For CFO NPs in this work and consistent with previous studies,[24] M_S, M_r, and H_C decrease with increasing OA. However, the squareness ratio ($R = M_r/M_S$) increases (at 10 K) from 0.58 to 0.82 with increasing particle size. The observed high R-value suggests the leaning toward cubic anisotropy with particle size. The R-values 0.82 (for S1) and 0.68 (for S2) are very close to CFO with a cubic anisotropy, where K1 > 0 (0.83) and K1 < 0 (0.87).[15] CFO NPs fluid also exhibits similar behavior.[61] Different types of intergrain group exchanges exhibit certain R-value; for R < 0.5, the particle can interact by magnetostatic interaction, and for R = 0.5, it is randomly oriented noninteracting particles that undergo coherent rotations.[2] Finally, 0.5 < R < 1.0 confirms the existence of exchange coupling. According to this criterion, at 10 K, the dominance

DOI: 10.1021/acsanm.8b02009
ACS Appl. Nano Mater. 2019, 2, 1828−1843

Table 6. Magnetic data for S1 sample before and after heating at 360 °C

	temp (K)	M_S (emu/g)	M_S (μ_B/F.U.)	M_r (emu/g)	H_C (Oe)	H_{ex} (Oe)	K_E (erg/cm^3)	H_{dip} (Oe)
$S1_{before}$	10	91.88	3.86	75.66	8823.36	39.345	6.74×10^6	49.56
	300	87.37	3.67	27.27	530.49	6.335	3.86×10^5	824.39
	385	77.85	3.27	19.73	261.54	9.045	1.69×10^5	1672.14
$S1_{T360}$	10	77.155	3.24	63.175	12236.07	13.955	7.85×10^6	35.74
	300	71.525	3.00	28.39	1140.025	43.935	6.78×10^5	383.63

of exchange coupling is clear, whereas at 385 K particles can interact by magnetostatic interaction.

Furthermore, coercivity (H_C) values of S1, S2, and S3 at 10 K were observed as 8.82 kOe, 8.55 kOe, and 7.11 kOe which are remarkably higher compared to bulk CFO (~5 kOe at 5 K).[62] Also, increasing OA content decreases H_C. Since the nanoparticle size monitors the coercivity, the H_C/D_{XRD} values were estimated as a function of OA concentration (Figure 10d). The results follow the similar trends, with S3 presenting the highest H_C/D_{XRD} values at 10 K, which verify that the particle size can control H_C. Moreover, H_C is very sensitive to the NP size, distribution characteristics, morphology, surface spin, and interparticle interaction. In the present study, the effective anisotropy, different exchange couple interaction, and interactions between the nanostructure are the predominant factors that influence H_C. Also, $H_C = 0.64K_E/M_S$, where K_E is the effective anisotropy constant, is valid for noninteracting, randomly oriented spherical NPs with cubic anisotropy. K_E values (Table 5) calculated using this relation also increase with particle size. Therefore, H_C, M_S, and K_E indicate that the increasing particle-size increases magnetic anisotropy, suggesting that the surface component of anisotropy plays a minor role. For an ensemble of NPs, the arrangement of NPs influences the nature and strength of interparticle interactions. The strength of dipolar interparticle interactions is estimated by the maximum dipolar field H_{dip} between nearest neighbor particles. $H_{dip} = 2\ \mu/d^3$, where "μ" is the particle moment ($\mu = M_S \times V_m$) and "d" is the distance between the centers of two particles.[63] It is noted that with an increase in OA concentration, the dipolar interparticle interaction also increases (at 10 and 385 K). At 385 K, H_{dip} rapidly increases as compared to 10 K because of the larger magnetic grain size at different OA concentrations. Finally, for sample S1, we probed the evolution of dipolar interparticle interactions with thermal treatments to clarify the role of OA as a surfactant. The S1 sample is heated at 360 °C to decompose the OA from CFO NPs, and the parameters obtained are presented in Table 6.

Figure 11 shows the M-H loops for S1 sample before and after thermal treatment. For S1 sample before heating ($S1_{before}$), H_{dip} is about 824.39 Oe (at 300 K) and 49.56 Oe (at 10 K), while for $S1_{T360}$ the strength of dipolar interparticle interactions decrease to 383.63 and 35.74 Oe at 300 and 10 K, respectively. As expected, the molecular coating plays a major role in tuning the dipolar interparticle interactions. Notice that $S1_{T360}$ sample shows the increase of H_{dip} from 35.74 Oe (10 K) to 383.63 Oe (300 K). The combined effect of particle-size decrease and enhanced dipolar interparticle interactions with OA induces a strong increase of the mean T_B, as confirmed by ZFC−FC measurements. Magnetic anisotropy of MNPs is typically related to surface component (K_S). Generally, particle size reduction enhances K_S, which in turn increases magnetic anisotropy. On the contrary, for the present case of OA-based solvothermally produced CFO NPs, anisotropy increases with

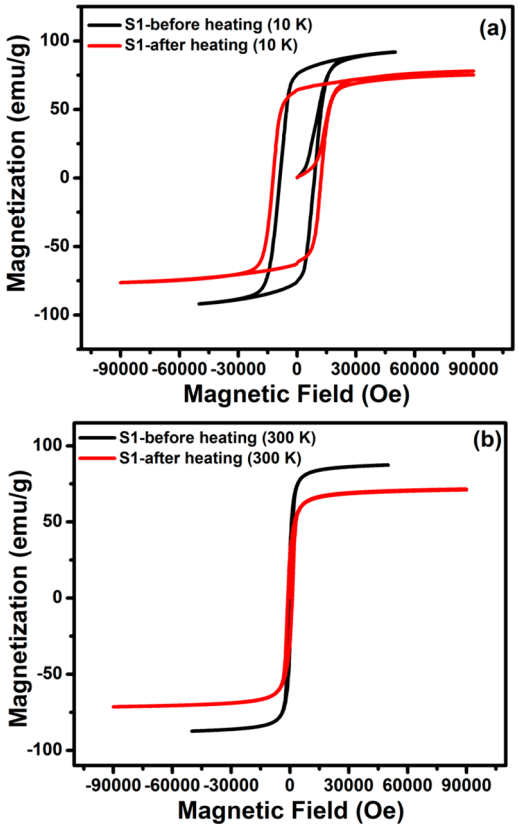

Figure 11. M-H loops measured for S1 sample before and after heat treatment (360 °C) at 10 K (a) and 300 K (b).

size indicating that the magnetocrystalline component plays the key role. In fact, Fe_3O_4 and CFO NPs synthesized using organic precursors also exhibit the similar behavior.[15,22] In order to understand the overall effect of OA concentration, the evolution of magnetic properties with thermal treatments for the sample S1 appears extremely useful. The key role played by the molecular coating is evident in S1 upon thermal treatment, which induces strong increase of surface component of anisotropy due to OA decomposition. Also, M_S decrease is compatible with thermal treatment induced variation in cationic distribution.[63−65] Spin−orbit coupling governs the magnetic anisotropy; thus, the spin−orbit coupling becomes smaller when nanoparticle metal cations are coordinated with OA. The net result is the reduction in surface anisotropy and coercivity of CFO NPs as evident from Tables 5 and 6. Despite the fact that surface usually exhibits some degree of spin disorder, presence of covalent bonded OA coating influences the symmetry and crystal field of metal ion closely resembling that of the core.[66,67] Therefore, in addition to reducing spin disorder, OA coating causes hindering of interface exchange coupling between ordered core and magnetically disordered shell.[67]

DOI: 10.1021/acsanm.8b02009
ACS Appl. Nano Mater. 2019, 2, 1828−1843

IV. CONCLUSIONS

Surface functionalization of CFO nanoparticles with different concentration of oleic acid (OA) provides the ability to design novel nanostructured magnetic materials. Fundamentally, as revealed in these studies, OA helps to control the particle size of CFO NPs; particle-size reduction occurs with increasing OA concentration. XPS and EDS data confirm that the synthesized CFO NPs were chemically homogeneous with Fe and Co in their chemical valence states of +3 (Fe^{3+}) and +2 (Co^{2+}), respectively. FTIR and Raman data further validate the chemical quality and bonding, in addition to surface OA interaction, in CFO NPs. The interaction between OA and surface atoms of CFO leads to a strong modification of anisotropy and interparticle interactions. The magnetic studies showed a significant increase in magnetic anisotropy for CFO NPs with a corresponding particle size reduction from 15 to 7 nm. Magnetic studies further confirm that the magnetic anisotropy is dominated by the magnetocrystalline component over the surface component. Raman scattering also revealed blue shift and peak broadening, which are interlinked with surface modification, enhanced magnetic ordering, and size reduction of CFO NPs. Comparison of magnetic properties for as-synthesized and thermally treated CFO NPs provides the fundamental insights into the overall effect of OA concentration. Interparticle interactions are enhanced in thermally treated CFO NPs due to the elimination of surfactant, while particle-size-increase effect is minimal. Presence of covalent bonded OA coating influences the symmetry and crystal field of metal ion closely resembling that of the core. In addition to reducing spin disorder, OA molecular coating causes hindering of interface exchange coupling between ferromagnetically ordered core and magnetically disordered shell as is evident in magnetic studies of thermally treated CFO NPs.

■ ASSOCIATED CONTENT

Supporting Information

The Supporting Information is available free of charge on the ACS Publications website at DOI: 10.1021/acsanm.8b02009.

Additional details of the FESEM micrographs, fundamental SAXS theory with equation, EDS data, XRD refinement data, and structural information, FTIR absorption bands, and XPS (PDF)

■ AUTHOR INFORMATION

Corresponding Authors

*Y.D.K.: e-mail, ydkolekar@gmail.com.
*C.V.R.: e-mail, rvchintalapalle@utep.edu.

ORCID

Chintalapalle V. Ramana: 0000-0002-5286-3065

Notes

The authors declare no competing financial interest.

■ ACKNOWLEDGMENTS

S.M.A. is thankful to BARC for providing the financial assistance (Grant GOI-E-175) to carry out the research work. Also, we are thankful to Dr. R. S. Devan, Metallurgy Engineering and Materials Science, Indian Institute of Technology (IIT), Indore, for help with the FE-SEM images. The authors are also thankful to Vishal Zade, Research Associate at the Center for Advanced Materials Research (CMR) at the University of Texas at El Paso, for his assistance in designing a professional cover page illustration based on the data presented in this paper. C.V.R. acknowledges with pleasure the support from the National Science Foundation (NSF), U.S., with NSF-PREM Grant DMR-1827745.

■ REFERENCES

(1) Ansari, S. M.; Bhor, R. D.; Pai, K. R.; Mazumder, S.; Sen, D.; Kolekar, Y. D.; Ramana, C. V. Size and Chemistry Controlled Cobalt-Ferrite Nanoparticles and Their Anti-proliferative Effect against the MCF-7 Breast Cancer Cells. *ACS Biomater. Sci. Eng.* **2016**, *2*, 2139−2152.

(2) Cai, B.; Zhao, M.; Ma, Y.; Ye, Z.; Huang, J. Bioinspired Formation of 3D Hierarchical $CoFe_2O_4$ Porous Microspheres for Magnetic-Controlled Drug Release. *ACS Appl. Mater. Interfaces* **2015**, *7*, 1327−1333.

(3) Ansari, S. M.; Suryawanshi, S. R.; More, M. A.; Sen, D.; Kolekar, Y. D.; Ramana, C. V. Field Emission Properties of Nano-structured Cobalt Ferrite ($CoFe_2O_4$) Synthesized by Low-temperature Chemical Method. *Chem. Phys. Lett.* **2018**, *701*, 151−156.

(4) Georgiadou, V.; Makris, G.; Papagiannopoulou, D.; Vourlias, G.; Dendrinou-Samara, C. Octadecylamine Mediated Versatile Coating of $CoFe_2O_4$NPs for the Sustained Release of Anti-inflammatory Drug Naproxen and in Vivo Target Selectivity. *ACS Appl. Mater. Interfaces* **2016**, *8*, 9345−9360.

(5) Kumar, P. A.; Ray, S.; Charkraverty, S.; Sarma, D. D. Engineered Spin-Valve Type Magnetoresistance in Fe_3O_4-$CoFe_2O_4$ Core-Shell Nanoparticles. *Appl. Phys. Lett.* **2013**, *103*, 102406.

(6) Shenker, H. Magnetic Anisotropy of Cobalt Ferrite ($Co_{1.01}Fe_{2.00}O_{3.62}$) and Nickel Cobalt Ferrite ($Ni_{0.72}Fe_{0.20}Co_{0.08}Fe_2O_4$). *Phys. Rev.* **1957**, *107*, 1246.

(7) Liu, X. L.; Wang, Y. T.; Ng, C. T.; Wang, R.; Jing, G. Y.; Yi, J. B.; Yang, J.; Bay, B. H.; Yung, L. Y. L.; Fan, D. D.; Ding, J.; Fan, H. M. Coating Engineering of $MnFe_2O_4$Nanoparticles with Superhigh T2 Relaxivity and Efficient Cellular Uptake for Highly Sensitive Magnetic Resonance Imaging. *Adv. Mater. Interfaces* **2014**, *1* (1−12), 1300069.

(8) Liu, X. L.; Fan, H. M.; Yi, J. B.; Yang, Y.; Choo, E. S. G.; Xue, J. M.; Fan, D. D.; Ding, J. Optimization of Surface Coating on Fe_3O_4 Nanoparticles for High Performance Magnetic Hyperthermia Agents. *J. Mater. Chem.* **2012**, *22*, 8235−8244.

(9) Khanra, S.; Abdullah-Al Mamun, Md.; Ferreira, F. F.; Ghosh, K.; Guha, S. Functionalized Self-Assembled Peptide Nanotubes with Cobalt Ferrite Nanoparticles for Applications in Organic Electronics. *ACS Appl. Nano Mater.* **2018**, *1*, 1175−1187.

(10) Jung, J. H.; Kim, S.; Kim, H.; Park, J.; Oh, J. H. High Performance Flexible Organic Nano-Floating Gate Memory Devices Functionalized with Cobalt Ferrite Nanoparticles. *Small* **2015**, *11*, 4976−4984.

(11) Lu, Y.; Yin, Y.; Mayers, B. T.; Xia, Y. Modifying the Surface Properties of Superparamagnetic Iron Oxide Nanoparticles through A Sol−Gel Approach. *Nano Lett.* **2002**, *2*, 183−186.

(12) Davies, R.; Schurr, G. A.; Meenan, P.; Nelson, R. D.; Bergna, H. E.; Brevett, C. A.; Goldbaum, R. H. Engineered Particle Surfaces. *Adv. Mater.* **1998**, *10*, 1264−1270.

(13) Mazario, E.; Sanchez-Marcos, J.; Menendez, N.; Canete, M.; Mayoral, A.; Rivera-Fernandez, S.; de la Fuente, J. M.; Herrasti, P. High Specific Absorption Rate and Transverse Relaxivity Effects in Manganese Ferrite Nanoparticles Obtained by an Electrochemical Route. *J. Phys. Chem. C* **2015**, *119*, 6828−6834.

(14) Parker, D.; Dupuis, V.; Ladieu, F.; Bouchaud, J. P.; Dubois, E.; Perzynski, R.; Vincent, E. Spin-glass Behavior in an Interacting γ-Fe_2O_3 Nanoparticle System. *Phys. Rev. B: Condens. Matter Mater. Phys.* **2008**, *77*, 104428−104429.

(15) Peddis, D.; Orru, F.; Ardu, A.; Cannas, C.; Musinu, A.; Piccaluga, G. Interparticle Interactions and Magnetic Anisotropy in Cobalt Ferrite Nanoparticles: Influence of Molecular Coating. *Chem. Mater.* **2012**, *24*, 1062−1071.

DOI: 10.1021/acsanm.8b02009
ACS Appl. Nano Mater. 2019, 2, 1828−1843

(16) Berkowitz, A. E.; Lahut, J. A.; Jacobs, I. S.; Levinson, L. M.; Forester, D. W. Spin Pinning at Ferrite-Organic Interfaces. *Phys. Rev. Lett.* **1975**, *34*, 594−597.
(17) Vestal, C. R.; Zhang, Z. J. Effects of Surface Coordination Chemistry on the Magnetic Properties of $MnFe_2O_4$ Spinel Ferrite Nanoparticles. *J. Am. Chem. Soc.* **2003**, *125*, 9828−9833.
(18) Tanaka, Y.; Saita, S.; Maenosono, S. Influence of Surface Ligands on Saturation Magnetization of FePt Nanoparticles. *Appl. Phys. Lett.* **2008**, *92*, 093117.
(19) Bødker, F.; Mørup, S.; Linderoth, S. Surface Effects in Metallic iron Nanoparticles. *Phys. Rev. Lett.* **1994**, *72*, 282−285.
(20) Ansari, S. M.; Bhor, R. D.; Pai, K. R.; Sen, D.; Mazumder, S.; Ghosh, K.; Kolekar, Y. D.; Ramana, C. V. Cobalt Nanoparticles for Biomedical Applications: Facile Synthesis, Physiochemical Characterization, Cytotoxicity Behavior and Biocompatibility. *Appl. Surf. Sci.* **2017**, *414*, 171−187.
(21) Guardia, P.; Batlle-Brugal, B. B.; Roca, A. G.; Iglesias, O.; Morales, M. P.; Serna, C. J.; Labarta, A.; Batlle, X. Surfactant Effects in Magnetite Nanoparticles of Controlled Size. *J. Magn. Magn. Mater.* **2007**, *316*, 756−759.
(22) Roca, A. G.; Morales, M. P.; O'Grady, K.; Serna, C. Structural and Magnetic Properties of Uniform Magnetite Nanoparticles Prepared by High Temperature Decomposition of Organic Precursors. *Nanotechnology* **2006**, *17*, 2783−2788.
(23) Perez, N.; Guardia, P.; Roca, A. G.; Morales, M. P.; Serna, C. J.; Iglesias, O.; Bartolome, F.; Garcia, L. M.; Batlle, X.; Labarta, A. Surface Anisotropy Broadening of the Energy Barrier Distribution in Magnetic Nanoparticles. *Nanotechnology* **2008**, *19*, 475704.
(24) Jovanovic, S.; Spreitzer, M.; Tramsek, K.; Trontelj, Z.; Suvorov, D. Effect of Oleic Acid Concentration on the Physicochemical Properties of Cobalt Ferrite Nanoparticles. *J. Phys. Chem. C* **2014**, *118*, 13844−13856.
(25) Gong, T.; Yang, D.; Hu, J.; Yang, W.; Wang, C.; Lu, J. Q. Preparation of Monodispersed Hybrid Nanospheres with High Magnetite Content from Uniform Fe_3O_4 Clusters. *Colloids Surf., A* **2009**, *339*, 232−239.
(26) Limaye, M. V.; Singh, S. B.; Date, S. K.; Kothari, D.; Reddy, V. R.; Gupta, A.; Sathe, A. V.; Choudhary, R. J.; Kulkarni, S. K. High Coercivity of Oleic Acid Capped $CoFe_2O_4$ Nanoparticles at Room Temperature. *J. Phys. Chem. B* **2009**, *113*, 9070−9076.
(27) Schmidt, P. W.; Hight, R., Jr. Slit height corrections in small angle X-ray scattering. *Acta Crystallogr.* **1960**, *13*, 480.
(28) Guinier, A.; Fournet, G.; Walker, B. C.; Yudowith, L. K. *Small Angle Scattering of X-rays*; Wiley: New York, 1955.
(29) Pedersen, J. S. Determination of Size Distribution From Small-angle Scattering Data for Systems with Effective Hard-sphere Interactions. *J. Appl. Crystallogr.* **1994**, *27*, 595−608.
(30) Yanez-Vilar, S.; Sanchez-Andujar, M.; Gomez-Aguirre, C.; Mira, J.; Senaris-Rodriguez, M. A.; Castro-Garcia, S. A Simple Solvothermal Synthesis of MFe_2O_4 (M=Mn, Co and Ni) Nanoparticles. *J. Solid State Chem.* **2009**, *182*, 2685−2690.
(31) Georgiadou, V.; Kokotidou, C.; Le Droumaguet, B.; Carbonnier, B.; Choli-Papadopoulou, T.; Dendrinou-Samara, C. Oleylamine as a Beneficial Agent for the Synthesis of $CoFe_2O_4$ Nanoparticles with Potential Biomedical Uses. *Dalton Trans.* **2014**, *43*, 6377−6388.
(32) Ayyappan, S.; Mahadevan, S.; Chandramohan, P.; Srinivasan, M. P.; Philip, J.; Raj, B. Influence of Co^{2+} Ion Concentration on the Size, Magnetic Properties, and Purity of $CoFe_2O_4$Spinel Ferrite Nanoparticles. *J. Phys. Chem. C* **2010**, *114*, 6334−6341.
(33) Ayyappan, S.; Gnanaprakash, G.; Panneerselvam, G.; Antony, M. P.; Philip, J. Effect of Surfactant Monolayer on Reduction of Fe_3O_4 Nanoparticles under Vacuum. *J. Phys. Chem. C* **2008**, *112*, 18376−18383.
(34) Wu, N.; Fu, L.; Su, M.; Aslam, M.; Wong, K. C.; Dravid, V. P. Interaction of Fatty Acid Monolayers with Cobalt Nanoparticles. *Nano Lett.* **2004**, *4*, 383−386.
(35) Nakamoto, K. *Infrared Spectra of Inorganic and Coordination Compounds*; Wiley: New York, 1963.
(36) Ayyappan, S.; Panneerselvam, G.; Antony, M. P.; Philip, J. High Temperature Stability of Surfactant Capped $CoFe_2O_4$ Nanoparticles. *Mater. Chem. Phys.* **2011**, *130*, 1300−1306.
(37) Lan, Q.; Chao, L.; Yang, F.; Liu, S.; Xu, J.; Sun, D. J. Synthesis of Bilayer Oleic Acid-Coated Fe_3O_4 Nanoparticles and Their Application in pH-responsive Pickering Emulsions. *J. Colloid Interface Sci.* **2007**, *310*, 260−269.
(38) Sharifi, I.; Shokrollahi, H.; Doroodmand, M. M.; Safi, R. Magnetic and Structural Studies on $CoFe_2O_4$ Nanoparticles Synthesized by Co-precipitation, Normal Micelles and Reverse Micelles Methods. *J. Magn. Magn. Mater.* **2012**, *324*, 1854−1861.
(39) Laha, S. S.; Regmi, R.; Lawes, G. Structural Origin for Low-temperature Relaxation Features in Magnetic Nanoparticles. *J. Phys. D: Appl. Phys.* **2013**, *46*, 325004.
(40) Datt, G.; Sen Bishwas, M.; Raja, M. M.; Abhyankar, A. C. Observation of Magnetic Anomalies in One-Step Solvothermally Synthesized Nickel-Cobalt Ferrite Nanoparticles. *Nanoscale* **2016**, *8*, 5200−5213.
(41) Macia, J.; Martin, E.; Perez-Rodriguez, A.; Jimenez, J.; Morante, J. R.; Aspar, B.; Margail, J. Raman Microstructural Analysis of Silicon-on-Insulator Formed by High Dose Oxygen Ion Implantation: As-implanted Structures, J. Margili. *J. Appl. Phys.* **1997**, *82*, 3730.
(42) Singh, J. P.; Srivastava, R. C.; Agrawal, H. M.; Kumar, R. Micro-Raman Investigation of Nanosized Zinc Ferrite: Effect of Crystallite size and Influence of Irradiation. *J. Raman Spectrosc.* **2011**, *42*, 1510−1517.
(43) Wegener, W.; Scheerlinck, D.; Legrand, E.; Hautecler, S.; Brabers, V. Inelastic Neutron Scattering Study Of Acoustical Magnons In $MnFe_2O_4$. *Solid State Commun.* **1974**, *15*, 345.
(44) Nappini, S.; Magnano, E.; Bondino, F.; Píš, I.; Barla, A.; Fantechi, E.; Pineider, F.; Sangregorio, C.; Vaccari, L.; Venturelli, L.; Baglioni, P. Surface Charge and Coating of $CoFe_2O_4$ Nanoparticles: Evidence of Preserved Magnetic and Electronic Properties. *J. Phys. Chem. C* **2015**, *119*, 25529−25541.
(45) Li, M.; Mao, Y.; Yang, H.; Li, W.; Wang, C.; Liu, P.; Tog, Y. Controllable Electrochemical Synthesis of $CoFe_2O_4$ Nanostructures on FTO Substrate and their Magnetic Properties. *New J. Chem.* **2013**, *37*, 3116−3120.
(46) Ammar, S.; Helfen, A.; Jouini, N.; Fiévet, F.; Rosenman, I.; Villain, F.; Molinié, P.; Danot, M. Magnetic Properties of Ultrafine Cobalt Ferrite Particles Synthesized by Hydrolysis in a Polyol Medium. *J. Mater. Chem.* **2001**, *11*, 186−192.
(47) Jaffari, G. H.; Ceylan, A.; Bui, H. P.; Beebe, T. P.; Ozcan, S. J.; Shah, S. I. Non-equilibrium Cation Distribution and Enhanced Spin Disorder in Hollow $CoFe_2O_4$ Nanoparticles. *J. Phys.: Condens. Matter* **2012**, *24*, 336004.
(48) Zhou, Z.; Zhang, Y.; Wang, Z.; Wei, W.; Tang, W.; Shi, J.; Xiong, R. Electronic Structure Studies of the Spinel $CoFe_2O_4$ by X-Ray Photoelectron Spectroscopy. *Appl. Surf. Sci.* **2008**, *254*, 6972−6975.
(49) Dupin, J. C.; Gonbeau, D.; Vinatier, P.; Levasseur, A. Systematic XPS Studies of Metal Oxides, Hydroxides and Peroxides. *Phys. Chem. Chem. Phys.* **2000**, *2*, 1319−1324.
(50) Cossaro, A.; Puppin, M.; Cvetko, D.; Kladnik, G.; Verdini, A.; Coreno, M.; de Simone, M.; Floreano, L.; Morgante, A. Tailoring SAM-on-SAM Formation. *J. Phys. Chem. Lett.* **2011**, *2*, 3124−3129.
(51) Wu, N.; Fu, L.; Su, M.; Aslam, M.; Wong, K. C.; Dravid, V. P. Interaction of Fatty Acid Monolayers with Cobalt Nanoparticles. *Nano Lett.* **2004**, *4*, 383−386.
(52) Wulser, K. W.; Langell, M. A. Carboxylic Acid Adsorption on NiO (100) Characterized by X-Ray Photoelectron and High Resolution Electron Energy Loss Spectroscopies. *Catal. Lett.* **1992**, *15*, 39−50.
(53) Bhowmik, R. N.; Kazhugasalamoorthy, S.; Ranganathan, R.; Sinha, A. K. Tuning of Composite Cubic Spinel Structure in $Co_{1.75}Fe_{1.25}O_4$ Spinel Oxide by Thermal Treatment and its Effects on Modifying the Ferrimagnetic Properties. *J. Alloys Compd.* **2016**, *680*, 315−327.

DOI: 10.1021/acsanm.8b02009
ACS Appl. Nano Mater. 2019, 2, 1828−1843

(54) Sinha, A. K.; Singh, M. N.; Achary, S. N.; Sagdeo, A.; Shukla, D. K.; Phase, D. M. Crystal Field Splitting and Spin States of Co Ions in Cobalt Ferrite with Composition $Co_{1.5}Fe_{1.5}O_4$ using Magnetization and X-ray Aabsorption Spectroscopy Measurements. *J. Magn. Magn. Mater.* **2017**, *435*, 87−95.
(55) Khomchenko, V.; Troyanchuk, I.; Szymczak, R.; Szymczak, H. Negative Magnetization in $La_{0.75}Nd_{0.25}CrO_3$ perovskite. *J. Mater. Sci.* **2008**, *43*, 5662−5665.
(56) *CRC Handbook of Chemistry and Physics*, 92nd ed.; CRC Press, 2011; pp 3−579.
(57) Bhowmik, R. N.; Panda, M. R.; Yusuf, S. M.; Mukadam, M. D.; Sinha, A. K. Structural Phase Change in $Co_{2.25}Fe_{0.75}O_4$ Spinel Oxide by Vacuum Annealing and Role of Coexisting CoO Phase on Magnetic Properties. *J. Alloys Compd.* **2015**, *646*, 161−169.
(58) Kumar, Y.; Yadav, K. L.; Manjusha, J.; Shah, R.; Kotnala, K. Study of Structural, Dielectric, Electric, Magnetic and Magnetoelectric Properties of $K_{0.5}Na_{0.5}NbO_3$ -$Ni_{0.2}Co_{0.8}Fe_2O_4$ Composites. *Ceram. Int.* **2017**, *43*, 13438−13446.
(59) Delille, F.; Dieny, B.; Moussy, J. B.; Guittet, M. J.; Gota, S.; Gautier-Soyer, M. G.; Marin, C. Study of the Electronic Paraprocess and Antiphase Boundaries as Sources of the Demagnetisation Phenomenon in Magnetite. *J. Magn. Magn. Mater.* **2005**, *294*, 27−39.
(60) Fu, J. C.; Zhang, J. L.; Peng, Y.; Zhao, J. G.; Tan, G. G.; Mellors, N. J.; Xie, E. Q.; Han, W. H. Unique Magnetic Properties and Magnetization Reversal Process of $CoFe_2O_4$ Nanotubes Fabricated by Electrospinning. *Nanoscale* **2012**, *4*, 3932−3936.
(61) Moumen, N.; Bonville, P.; Pileni, M. P. Control of the Size of Cobalt Ferrite Magnetic Fluids: Mössbauer Spectroscopy. *J. Phys. Chem.* **1996**, *100*, 14410−14416.
(62) Bhattacharyya, S.; Salvetat, J. P.; Fleurier, R.; Husmann, A.; Cacciaguerra, T.; Saboungi, M. L. One Step Synthesis of Highly Crystalline and High Coercive Cobalt-ferrite Nanocrystals. *Chem. Commun.* **2005**, 4818−4820.
(63) Xu, S. T.; Ma, Y. Q.; Zheng, G. H.; Dai, Z. H. Simultaneous Effects of Surface Spins: Rarely Large Coercivity, High Remanence Magnetization and Jumps in the Hysteresis Loops Observed in $CoFe_2O_4$ Nanoparticles. *Nanoscale* **2015**, *7*, 6520−6526.
(64) Peddis, D.; Cannas, C.; Piccaluga, G.; Agostinelli, E.; Fiorani, D. Spin-glass-like Freezing and Enhanced Magnetization in Ultra-small $CoFe_2O_4$ Nanoparticles. *Nanotechnology* **2010**, *21*, 125705.
(65) Cannas, C.; Musinu, A.; Piccaluga, G.; Fiorani, D.; Peddis, D.; Rasmussen, H. K.; Mørup, S. Magnetic Properties of Cobalt ferrite-silica Nanocomposites Prepared by a Sol-gel Autocombustion Technique. *J. Chem. Phys.* **2006**, *125*, 164714.
(66) Cannas, C.; Musinu, A.; Ardu, A.; Orru, F.; Peddis, D.; Casu, M.; Sanna, R.; Angius, F.; Diaz, G.; Piccaluga, G. $CoFe_2O_4$ and $CoFe_2O_4/SiO_2$ Core/Shell Nanoparticles: Magnetic and Spectroscopic Study. *Chem. Mater.* **2010**, *22*, 3353−3361.
(67) Nogues, J.; Skumryev, V.; Sort, J.; Stoyanov, S.; Givord, D. Shell-Driven Magnetic Stability in Core-Shell Nanoparticles. *Phys. Rev. Lett.* **2006**, *97*, 157203−157204.

DOI: 10.1021/acsanm.8b02009
ACS Appl. Nano Mater. 2019, 2, 1828−1843